

An Architecture for Fast and Accurate Control of Shape Memory Alloy Actuators

Yee Harn Teh
Dept. Information Engineering
Australian National University
Canberra ACT 0200, Australia

Roy Featherstone
Dept. Information Engineering
Australian National University
Canberra ACT 0200, Australia

Abstract

This paper presents a new control architecture for fast, accurate force control of antagonistic pairs of shape memory alloy wires. The main components are: a differential-mode controller, which controls the output force, an anti-slack mechanism, a rapid-heating mechanism and an anti-overload mechanism. The closed-loop response is fast and accurate, even in the presence of large external motion disturbances. There is no sign of limit cycles; and the performance is unaffected by large load inertias. This paper also presents an architecture for position control, in which a position feedback loop is added to the force control architecture. Experimental results show force control accuracies as high as 1mN in a $\pm 3\text{N}$ range, force output rates as high as 50Ns^{-1} , and highly accurate position control with steady-state errors below the resolution of the position encoder.

1 Introduction

Wires made of Shape Memory Alloy (SMA) can be stretched easily when cool, but will contract forcefully back to their original length when heated. This effect can be harnessed to make actuators for robots and other mechanical devices. SMA actuators are well adapted for flexible and miniaturised force control applications due to their high force-to-weight ratio, mechanical simplicity, compactness, as well as silent, clean operation. Force control applications are very important for robotics, and they include robotic grippers and medical devices, as well as force contact applications. However, SMA actuators have disadvantages, including energy inefficiency, slow speed and inaccurate response. Most SMA robotic applications remain in the research and experimental phase.

In this paper, we present our research on SMA force and position control architectures, using an actuator based on an antagonistic pair of SMA wires. The force control architecture consists of a differential controller, an anti-slack mechanism, a rapid-heating mechanism, and an anti-overload mechanism. Our results show fast and very accurate responses to force commands with no sign of limit cycles. In particular, the rapid-heating mechanism allows the safe delivery of very large heating powers without the risk of overheating, by calculating a safe upper limit to the instantaneous heating power from measurements of electrical resistance. This allows the control system to achieve a maximum force rate of 50Ns^{-1} . This speed is achieved without compromising the setpoint accuracy, with error amplitudes at steady-state of only 0.001N. The possibility of actuator damage due to overheating and overstressing has been minimised using effective control algorithms such as the rapid-heating and anti-overload mechanisms. The force control architecture forms the inner loop in the proposed two-loop position control system. This control system achieves highly accurate responses with no limit cycles in the presence of large load inertias. The research described in this paper can be utilised for practical SMA actuator and robotic applications.

An outline of the paper is first provided. Section 2 contains some background information about SMA as well as a review of past research aimed at improving the performance of SMA actuators. In Section 3, the experimental test bed used for all of the experimental work is described. Section 4 describes the complete architecture of the differential force control system as well as the experimental results. In Section 5, experimental results are presented to demonstrate good rejection of external motion disturbances and load inertias. Finally, in Section 6, we propose a new two-loop position control architecture with a fast inner force loop

⁰The final, definitive version of this paper has been published in the International Journal of Robotics Research, vol. 27, no. 5, May 2008 by Sage Publications Ltd. All rights reserved. © SAGE Publications Ltd. 2008. It is available at <http://online.sagepub.com/>

based on the differential force controller and a slower outer position loop. Experimental results with the SMA actuator under heavy external loads are presented.

2 Background

Shape Memory Alloy exhibits a *shape memory effect*, which is the result of a phase transformation between a martensite crystal structure, which predominates at low temperatures, and an austenite crystal structure, which predominates at higher temperatures. The martensite phase has a low yield strength, and is easily deformed. However, the original shape of the material is recovered when it is heated, as the deformed martensite transforms into undeformed austenite. The phase transformation is nonlinear, and exhibits large thermal hysteresis.

The shape memory effect is the basis of actuator applications for SMA. There are two main types of the shape memory effect:

1. One-way shape memory effect — At the martensite phase, the alloy can be easily stretched using an external force. After removal of the force, the alloy shows permanent deformation. It can recover its original shape upon heating. Subsequent cooling does not change the shape unless it is stressed again.
2. Two-way shape memory effect — In addition to the one-way effect, shape change occurs upon cooling and without the applying of external stress. The SMA usually needs to be trained to exhibit the two-way effect.

Heating the SMA actuators can be done via Joule heating, which is resistively heating the actuators using electric current. SMA actuators can be used in various configurations including helical springs, cantilever strips, straight wires, torsion tubes and torsion springs (Waram, 1993). Because SMA actuators can only contract in one direction, it is necessary to provide a biasing force to return them to the neutral position. This can be accomplished using a dead weight, a bias spring, or another SMA element in a differential arrangement. In practice, the latter two arrangements are usually used. SMA actuator applications include linear actuators, micro-switches, micro-valves, robotic grippers, vibration control and active damping of structures, medical endoscopes and micro-electro-mechanical systems (MEMS) (Fu et al., 2004; Ikuta et al., 1988; Kohl, 2004; Liang and Rogers, 1993; Van Humbeeck, 1999).

Pioneering research on SMA actuators and material treatment included Bergamasco et al. (1990) and Hunter et al. (1991) in the early 1990s. More recent works on SMA control included Dickinson and Wen (1998), Elahinia and Ashrafioun (2002), Madill and Wang (1998), Moallem and Lu (2005), and Troisfontaine et al. (1997). However, a lot of these works failed to address crucial practical issues for robotic applications, namely, speed and accuracy of response, external load and motion disturbance rejection, overheating as well as overloading of the SMA actuators. For practical SMA actuator applications, these concerns should be appropriately addressed.

Some researchers have tried to improve the speed and accuracy of SMA response. One of the earliest attempts at improving SMA actuator speed is by Kuribayashi (1991). His method involved using miniature thermocouples to measure the temperatures of 0.5 mm antagonistic SMA wires and determining the heating currents based on a temperature threshold to prevent overheating. Improvements were demonstrated with moderate settling times of 0.2s for step responses, and stable sine responses at up to 0.4Hz, for angular displacements of 15° magnitude. Gorbet and Russell (1995); Russell and Gorbet (1995) worked on two fronts of the speed problem — rapid heating and improved cooling of SMA wires in antagonistic arrangement. To allow rapid heating without the danger of overheating, they used a non-contact infrared temperature sensing unit to measure the temperature and determine the currents to be delivered to the actuators. To improve cooling, they attached a mobile heat sink to help cool the passive actuator.

Grant and Hayward (1997a,b, 2000); Grant (1999) have made major contributions in improving the speed and accuracy of SMA actuators. They designed a novel SMA actuator comprised of 12 SMA wires in a helical arrangement that produced larger strains than long, straight SMA wires, but at the expense of reduced force outputs. Using the actuators in antagonistic arrangement, they investigated the use of two-stage relay control, which is a form of variable structure control (VSC). The results demonstrated fast and accurate force and position responses with 0.1s rise times for large force steps of 7N and position steps of 2.5mm, as well as stable tracking of both 2N and 1.5mm amplitude sine commands at 2Hz. One major problem they faced was the existence of limit cycles, or oscillations, due to the discontinuous switching of the relay controller. Grant and Hayward (1997a) managed to address this problem using a dead band controller in their control system under the 'no load' condition. Grant further extended this work in the presence of a load disturbance in Grant (1999), and although the limit cycles had been reduced, they were not completely eliminated. However, in all of their work, there had been no consideration about the overheating and overstressing of the actuators. Van

der Wijst (1998), as well as our previous work in Teh and Featherstone (2004), had also not been completely successful in preventing the limit cycles.

Ashrafiuon et al. (2006) further investigated the use of VSC in SMA position control. Their test bed consisted of a 3-link SMA actuated robot with a heavy payload. Results showed accurate position control, but with a slow rise time of 1s for a 70° magnitude step. Choi et al. (2001) also investigated the force control of an SMA-actuated flexible gripper based on H_∞ -controllers, but the resulting speed and accuracy of response were not impressive. Zhong and Yeong (2006) experimented with SMA wire-actuated grippers for miniature applications. They showed that cheap SMA actuators compared to other technologies such as piezoelectric actuators can produce large gripping forces reliably over millions of cycles.

3 Experimental Hardware

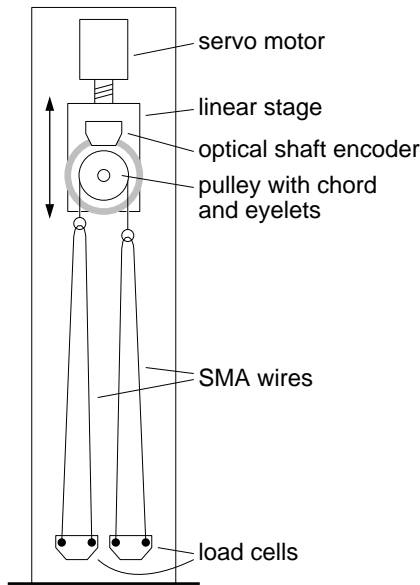


Figure 1: The mechanical part of the experimental test bed. Other components, which are not shown, include amplifiers, power supplies and a PC containing the dSPACE DS1104 real-time control board.

The experiments reported in this paper were conducted using the test bed shown in Figure 1. (The diagram is not drawn to scale.) The mechanical part consists of a metal column with a pair of load cells near the bottom and a linear stage, operated by a servo motor, near the top.¹ The stage provides precise vertical positioning of a shaft carrying a pulley and a high-resolution optical shaft encoder. A short length of aramid chord is fixed to the pulley, and terminates in two eyelets. Two lengths of Flexinol² wire are connected between the load cells and the eyelets, such that the two ends of each wire are connected to a load cell and the middle passes through an eyelet.

Flexinol wires are made from a nickel-titanium SMA called nitinol, and they have the special property that they can contract millions of times without fatigue, provided the working strain is limited to 4%. The wires in the test bed have a diameter of 0.1mm and an austenite finish temperature of 90°C . The wires are 80cm long, and they have a maximum pulling force of 1.5N. However, as they are physically folded in half, they are mechanically equivalent to a pair of 40cm wires in parallel. Thus, the maximum pulling force at each eyelet is 3N, and the maximum movement (for a 4% strain in the wire) is 1.6cm.

The load cells measure forces in the range of $\pm 9\text{N}$ at a resolution of 0.3mN and a bandwidth of 140Hz. The optical shaft encoder has a resolution of 8192 bits per revolution, and the pulley has a diameter of 1.6cm, so one encoder bit equates to approximately $6\mu\text{m}$ movement of an eyelet. The vertical positioning resolution of the linear stage is also about $6\mu\text{m}$.

Depending on the type of experiment to be performed, the pulley can either be locked in a single orientation, or allowed to rotate freely. In the experiments described in Sections 5 and 6, a pendulum weighing 79g is attached to the shaft, and serves as a large inertial load. In all other experiments, the pulley is locked.

¹The stage is a mini posi-drive (with custom motor mount) from Del-Tron; the motor is a Pittman brushless DC servo motor type 3441S002-r3; and the load cells are type S215 (2lb-force) from Strain Measurement Devices.

²Flexinol is a trademark of Dynalloy, Inc. (<http://www.dynalloy.com>)

Other components of the test bed include precision transconductance amplifiers that can deliver heating currents up to 0.8A to the SMA wires, and a DS1104 real-time control board from dSPACE, which can be programmed to implement any desired control system. In the experiments reported here, the DS1104 ran at a sampling rate of 5kHz.

4 Force Control Architecture

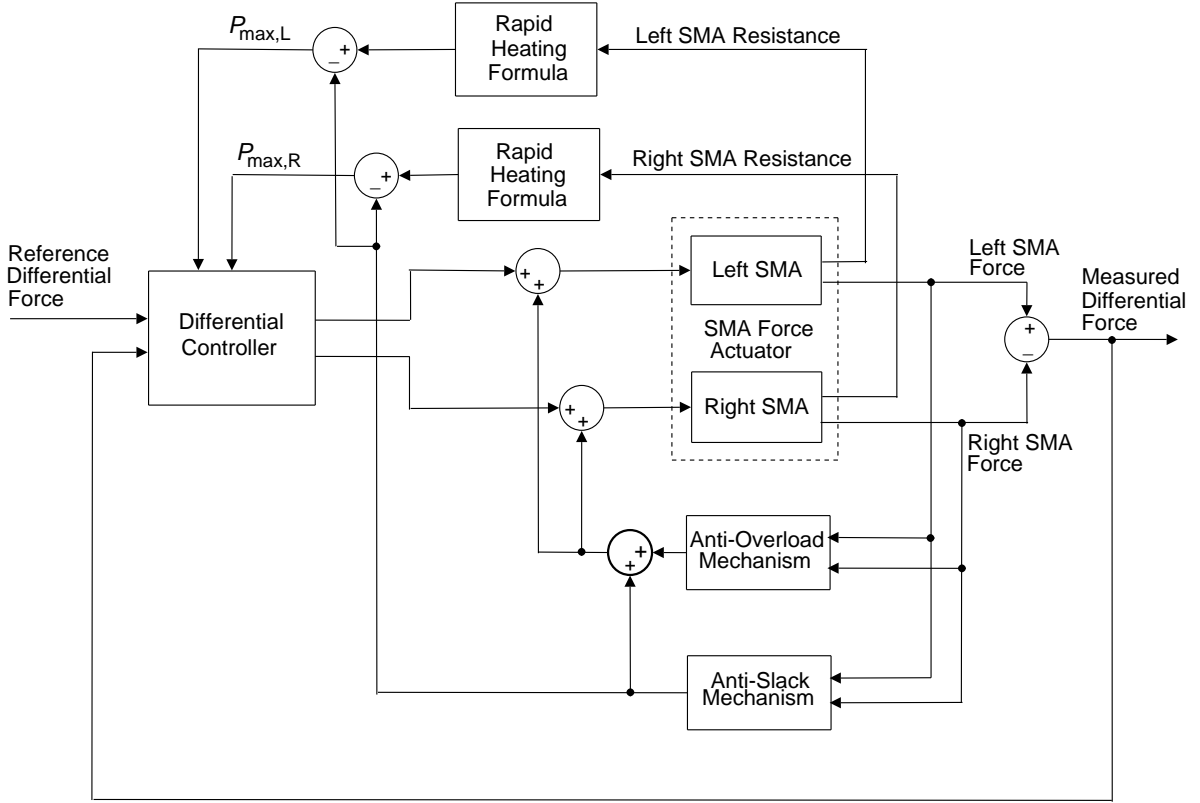


Figure 2: Overview of the force control system for an SMA actuator composed of an antagonistic pair of SMA wires.

Figure 2 shows the architecture of the force control system to produce fast, accurate responses in an actuator based on an antagonistic pair of SMA wires. Some details have been omitted for clarity. The main components of this control architecture are as follows.

1. As the actuator's output is the difference between the two SMA forces, the control system is organized into a differential channel and a common channel.
2. The differential controller is responsible for making the actuator's output force track the command input. The accuracy of the system as a whole depends on the accuracy of this controller.
3. The common channel is used to enforce upper and lower limits on the individual SMA forces. The anti-slack mechanism enforces the lower limit, and the anti-overload mechanism enforces the upper limit.
4. The whole control system operates within heating power limits that are calculated separately for each wire, based on its electrical resistance. A rapid-heating formula determines the maximum safe heating power for a given measured resistance; and these limits are fed back into the differential controller. This rapid-heating mechanism increases the actuator's safe maximum speed.

These components are described individually in the subsections that follow.

One of the missing details concerns the plant. The two boxes labelled 'Left SMA' and 'Right SMA' represent the plant, and the internal details of one of these boxes is shown in Figure 3. The power signal is first converted to a current signal, based on the power-current relationship, $P = I^2 R_{nom}$, where R_{nom} is a constant approximately equal to the resistance of the hot SMA wire. The DAC (Digital-to-Analog Converter) voltage is calculated from the current signal and the known gain of the transconductance amplifier which drives the SMA wire. The resistance of the SMA wire is estimated by combining a measurement of the voltage

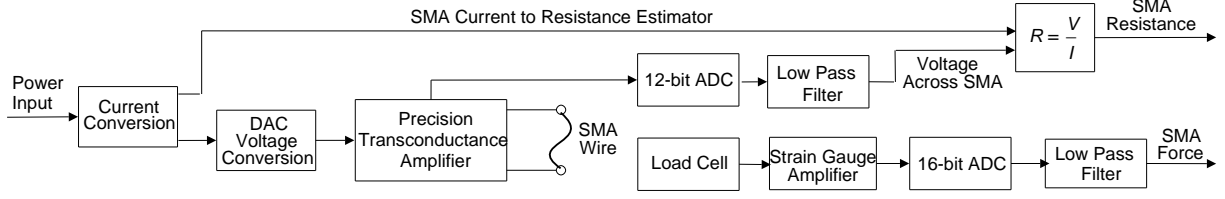


Figure 3: SMA Plant.

across the wire with the current signal. It is used for the rapid-heating calculations. The measured SMA force is determined from the load cell using a 16-bit ADC. The signals from the ADCs are low-pass filtered to filter out unwanted high-frequency noise. The force data presented in this paper has also been processed offline with a 4th-order, zero-phase, low-pass Butterworth filter (with cut-off frequency, $\omega_c = 200 \text{ rad s}^{-1}$).

4.1 Differential Controller

Figure 4 shows the block diagram of the differential controller. As can be seen, it consists of a PID controller, a dynamic saturation block,³ and an anti-windup circuit for the integrator. The dynamic saturation block prevents the output from exceeding the power levels determined by the rapid-heating formulae, and it allows the power levels, $P_{\max,L}$ and $P_{\max,R}$, to be set independently for the two SMA wires; the anti-windup circuit works correctly to reduce integrator overshoot and the control effort in the feedback system, even when the saturation function's limit values are time-varying signals. The output signal, P_{diff} , is a signed power signal. If P_{diff} is positive then it is sent to the left SMA, otherwise $-P_{\text{diff}}$ is sent to the right SMA. To avoid discontinuity in slope at $P_{\text{diff}} = 0$, soft-saturation blocks having the transfer function shown in Figure 5 are used to calculate the power to each wire.

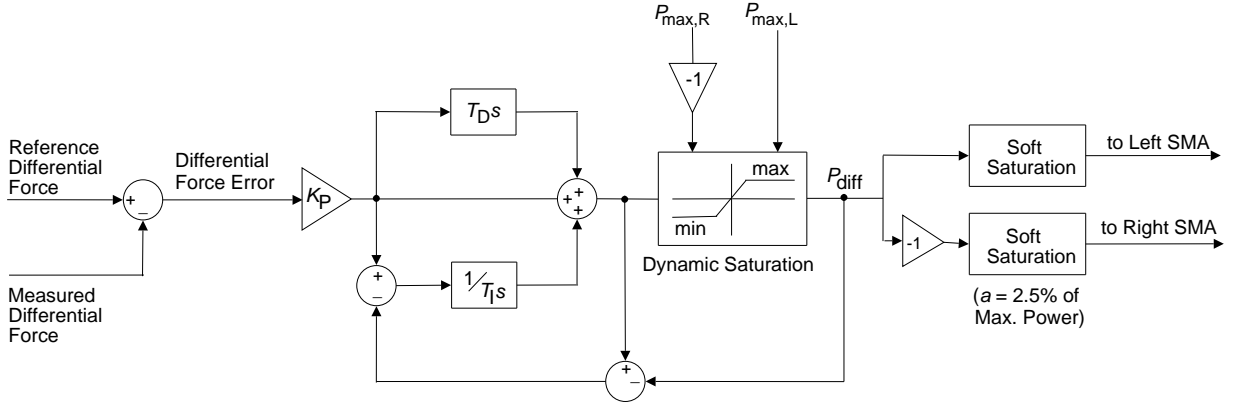


Figure 4: Differential PID controller with integrator anti-windup scheme and dynamic saturation.

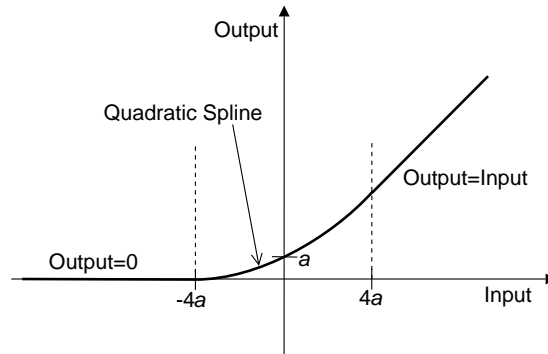


Figure 5: Soft saturation transfer function: a quadratic spline ensures continuity of slope.

³The saturation levels are allowed to vary with time, and are determined by the 'min' and 'max' inputs.

The PID controller transfer function is given by

$$D(s) = K_P(1 + \frac{1}{T_I s} + T_D s), \quad (1)$$

where K_P , T_I and T_D are the proportional, integral and derivative gains respectively. The PID parameter values are $K_P = 70$, $T_I = 0.0115$ and $T_D = 0.003$. The choice of a PID controller, and the choice of these particular parameter values, draws on the authors' past work, as described in Teh and Featherstone (2005, 2007a,b); Teh (2007). These papers prove that a high-frequency response exists in nitinol SMA; demonstrate that the high-frequency response can be measured and expressed as a set of gain/phase curves; fit a model to the measured data; report that a simulation based on this model predicts the onset of limit cycles in a PID force controller to within 10% of the true value; and report the parameters just mentioned as the result of an on-line tuning process that started with the parameter values suggested by the simulator.

The differential controller has a setpoint accuracy of better than 1mN, which is one part in 6000 of the 6N output force range of the actuator (-3N to $+3\text{N}$). Tracking errors are also small, as can be seen from the graphs later in this paper, and there are no limit cycles. The best comparable results in the literature can be found in Grant (1999), which have a setpoint accuracy of 40mN from the 7N force available from his SMA actuators. This is more than an order of magnitude worse than our accuracy measure.

4.2 Anti-Slack Mechanism

The Flexinol wires used in the experiments have been observed to develop a behaviour called the *two-way shape memory effect* during use. This effect is explained in Kohl (2004). Once this behaviour becomes entrained, the wires actively lengthen when cooled, even if the tension on them is zero. The end result is that the passive wire (the one that is not being heated) can develop a few millimetres of slack as it cools. This is not good for the control system — if a wire has gone slack then it cannot begin to pull until it has contracted enough to take up the slack. Slack in the wires can also lead to mechanical problems inside the actuator, such as entanglement, and possibly to electrical short-circuits.

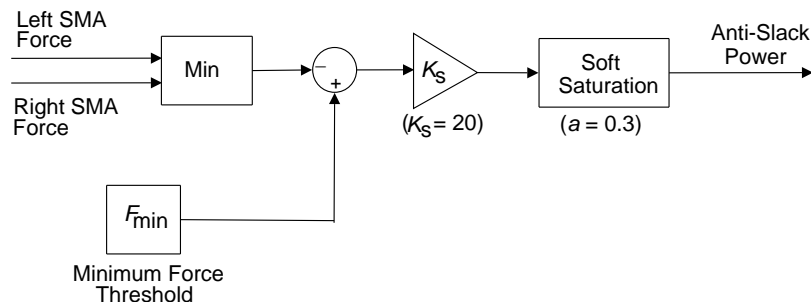


Figure 6: Anti-Slack Mechanism

To prevent the wires from going slack, the control architecture uses the anti-slack mechanism shown in Figure 6. It consists of a simple proportional feedback algorithm that uses the force outputs of the individual SMA wires, compares the minimum of the two forces to a minimum force threshold, F_{\min} , and appropriately determines an anti-slack power signal to make sure the lesser of the two SMA wire forces does not drop significantly below F_{\min} . The soft-saturation block, similar to the ones shown in Figure 4, allows for a smoother transition during the activation of the anti-slack mode. The anti-slack power is a common-mode signal as it is delivered to both SMA wires. The anti-slack mechanism is an improvement on a previous open-loop method of keeping the wires taut by means of a small positive bias power sent to each wire (Teh and Featherstone, 2004).

To illustrate the importance of the anti-slack mechanism, Figure 7 compares the experimental responses to $\pm 3\text{N}$ ramps with and without the anti-slack mechanism. In both sets of responses, the power levels of the dynamic saturation block ($P_{\max,L}$ and $P_{\max,R}$) are initially set to datasheet recommended levels (corresponding to 0.18A current). The experimental results without the anti-slack mechanism in Figures 7(a)–(d) is first discussed. As can be seen in Figure 7(d), at any instant, only one wire is being heated, while zero power is sent to the other wire (the passive wire). The passive wire becomes slack as it cools, and will therefore not begin to pull in response to heating current until it has contracted enough to become taut. This delay causes substantial tracking errors, which can be seen as kinks in Figure 7(a) and large spikes in Figure 7(b).

Figure 7(e) shows the improvements in experimental response to similar ramps of $\pm 3\text{N}$ with the anti-slack mechanism implemented. The anti-slack force threshold is set at 0.2N. Compared to the results in Figures 7(a)

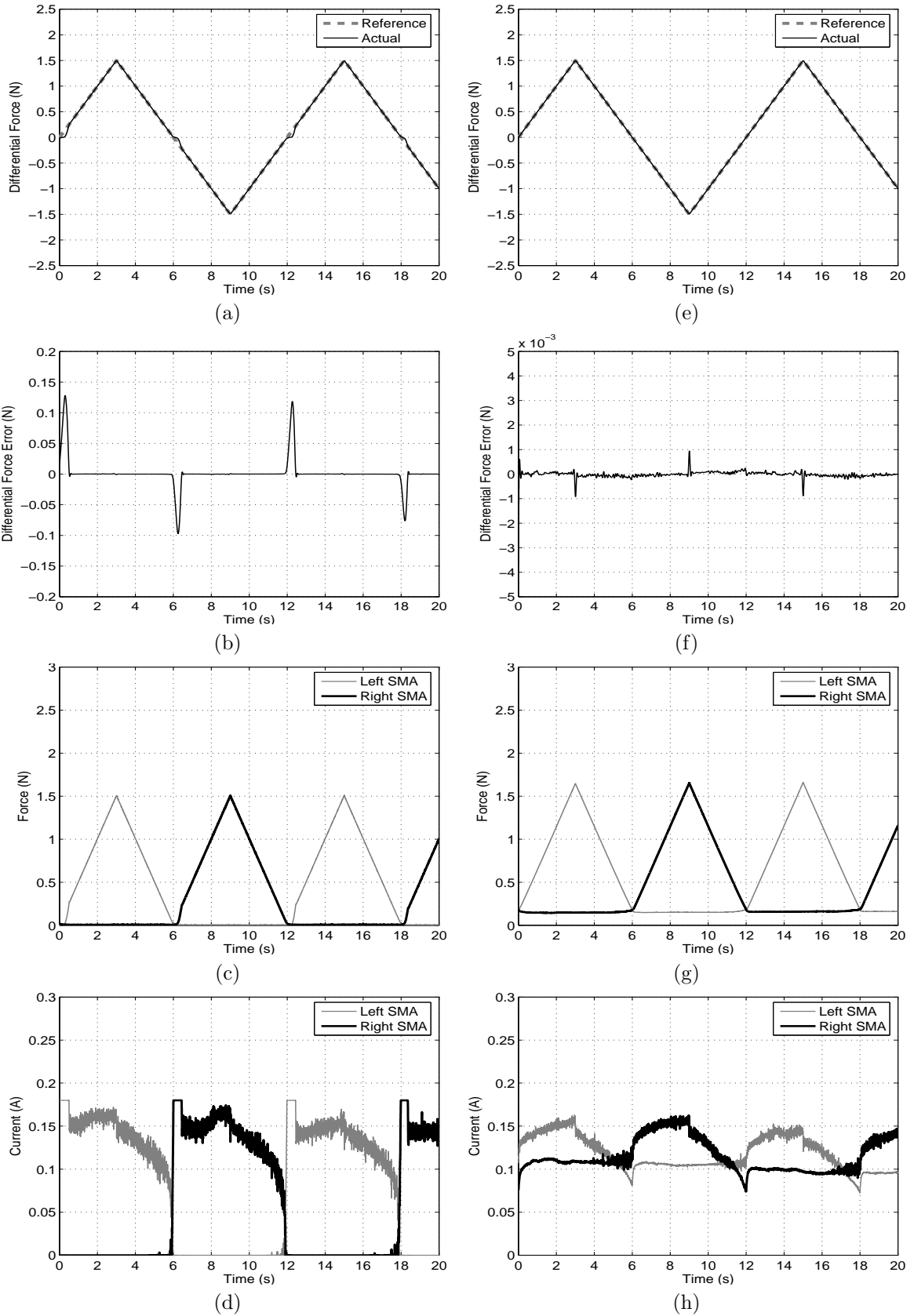


Figure 7: Comparison of experimental response for $\pm 3\text{N}$ ramps with and without anti-slack mechanism. (a) Differential force ramp response without anti-slack, (b) its corresponding force errors, (c) individual SMA forces, and (d) individual SMA heating currents. (e) Differential force ramp response with anti-slack, (f) its corresponding force errors, (g) individual SMA forces, and (h) individual SMA heating currents.

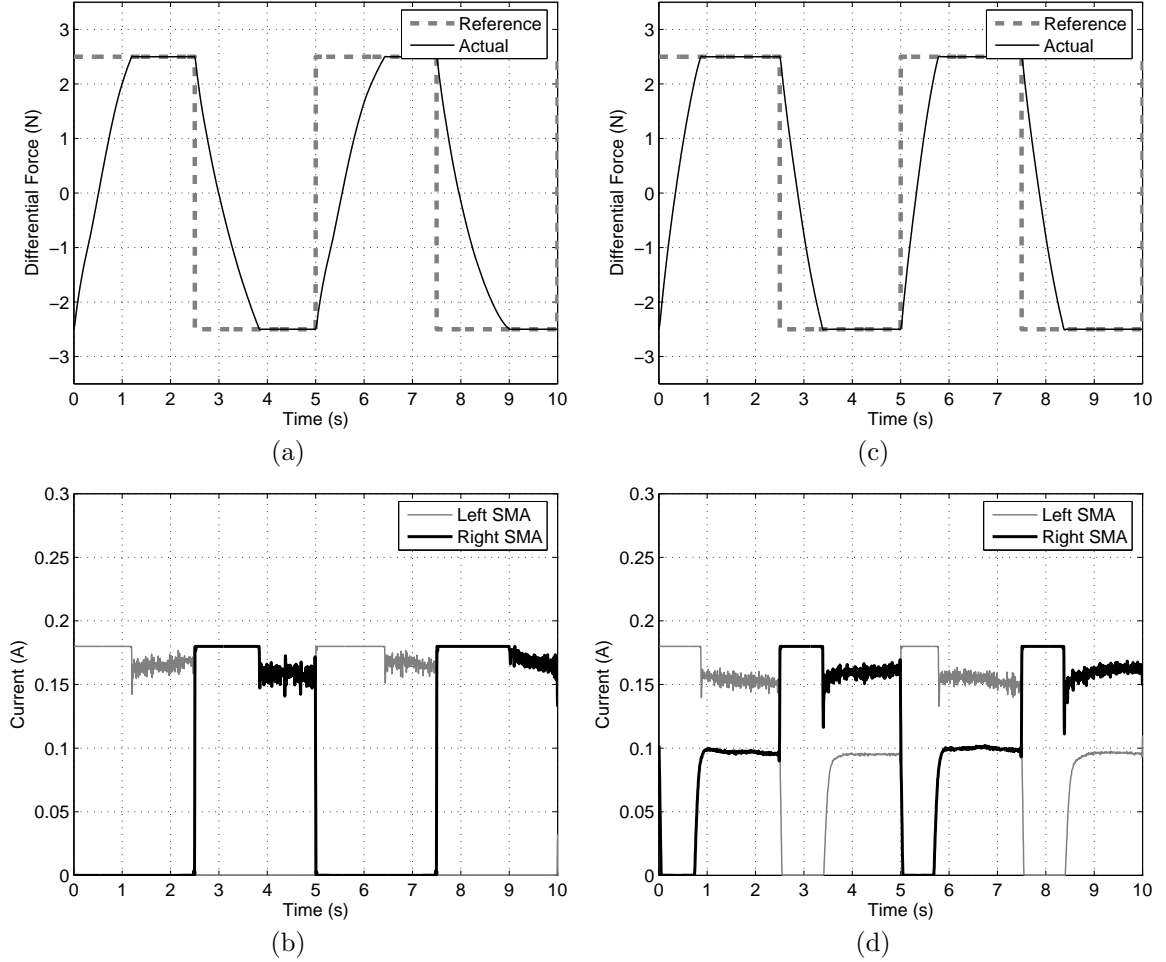


Figure 8: Comparison of experimental response for steps of $\pm 5\text{N}$ with and without anti-slack mechanism. (a) Differential force step response without anti-slack, and (b) its corresponding individual SMA heating currents. (c) Differential force step response with anti-slack, and (d) its corresponding individual SMA heating currents.

and 7(b), there are no large inaccuracies due to the passive wire becoming slack. High tracking accuracy with an error amplitude of less than 0.001N is achieved, except for a few spikes during the change in slopes. Note that the y-axis scale of Figure 7(f) is a factor of 40 larger than Figure 7(b). The anti-slack mechanism has demonstrated its effectiveness experimentally. The mechanism kicks in when the force on the cooling wire falls below 0.2N . Instead of heating one wire at any instant, as in Figure 7(d), a current of approximately 0.1A is applied to keep the wires warm and taut as can be seen in Figure 7(h).

Figure 8 compares the experimental responses to steps of $\pm 5\text{N}$ with and without the anti-slack mechanism. It can be observed that the response with anti-slack in Figure 8(c) is smoother and slightly faster than Figure 8(a), without anti-slack. Figure 8(d) clearly shows the anti-slack mechanism kicking in to heat the passive left SMA wire after 0.8s , then the passive right SMA wire after 3.5s , and so on. Despite the high accuracy at the steady-state, the speed of response of the actuator is slow, with rise times of about 0.8s for 5N magnitude steps. This is an average force rate of only 6.25Ns^{-1} . The limiting factor is the safe current level of 0.18A .

4.3 Rapid-Heating Mechanism

The rapid-heating mechanism sets an upper limit to the heating power that can be applied to each wire. The upper limit is calculated separately for each wire, and is a function of the wire's measured electrical resistance. The idea is to allow rapid heating of the wires, via large heating powers, whenever it is safe to do so, because rapid heating increases the speed of the actuator. The rapid-heating mechanism consists of the two blocks labelled 'rapid heating formula' in Figure 2, which calculate the power limits from the measured resistance, and the dynamic saturation block in Figure 4, which imposes the power limits on the controller. This section presents a full description of how the rapid-heating mechanism works, but more information can also be found

in Featherstone and Teh (2004, 2006).

The speed of an SMA actuator is determined partly by the rate at which the wires are heated, and partly by the rate at which they cool. According to the technical data sheets for nitinol wires (Dynalloy, 2007), the cooling rates for the thinnest wires are faster than the heating rates using the recommended heating currents.⁴ It is therefore possible to produce a substantial increase in the speed of an SMA actuator simply by using heating currents above the recommended values. However, the use of larger heating currents can raise the temperatures of the wires far above the transformation temperature range, with two adverse consequences: the wires take longer to cool, and they may suffer thermal damage.

One solution to this problem was proposed by Kuribayashi (1991). His method involves measuring the temperature of the wire directly using a thermocouple. If the temperature is below a chosen threshold, then a large heating current is allowed; otherwise, the current is switched off. The rapid-heating mechanism achieves a similar result, but without the use of a temperature sensor. Instead, it uses resistance as an indirect indication of temperature.

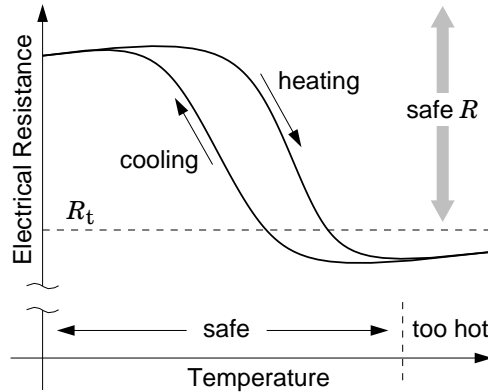


Figure 9: Electrical resistance of nitinol wire versus temperature

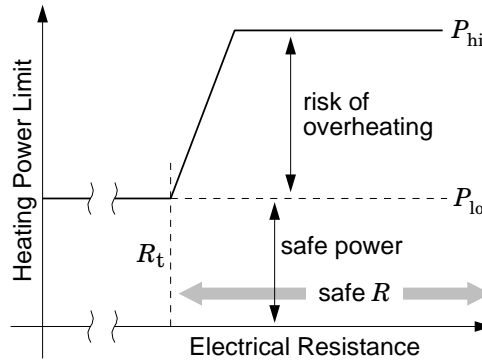


Figure 10: Heating power limit versus measured electrical resistance

Figures 9 and 10 show how the method works. Figure 9 shows a typical resistance-versus-temperature curve for a nitinol wire. The physical explanation for this curve is that the resistivity of the martensite crystal phase (in nitinol) is about 20% higher than the resistivity of the austenite phase. As a result, the resistance of the wire is about 20% higher when it is cold than when it is hot. Furthermore, the resistance varies with the martensite ratio,⁵ so it drops smoothly as the wire is heated, and rises smoothly again as it cools. The hysteresis shown in this figure is a consequence of the thermal hysteresis in the phase transformation.

The presence of hysteresis in the temperature/resistance relationship means that it is not possible to deduce the exact temperature of the wire from its resistance. Nevertheless, it is possible to identify a threshold resistance, R_t , with the property that if the measured resistance is greater than R_t then we can be certain that the wire is not too hot. In practice, a small safety margin should be built into the chosen value of R_t , so as to account for measurement errors and the variation of resistance with strain. In our experiments, a safety margin of 5% has been used.

⁴Specifying a heating current is equivalent to specifying a heating power per unit length of wire.

⁵a value between 0 and 1 denoting the proportion of the material currently in the martensite phase.

Let P_{\max} denote the maximum heating power for a single SMA wire. Figure 10 illustrates the calculation of P_{\max} from the measured electrical resistance, R . If $R < R_t$ then it is not possible to tell from the resistance whether or not the wire is overheating. P_{\max} is therefore set to a relatively low power level, P_{lo} , which is sufficiently low that it will not overheat the wire, even if applied indefinitely. Typically, P_{lo} is calculated from the data-sheet recommended heating current and the length of the wire. If $R \geq R_t$ then we can be sure that the wire is not overheating, so it is safe to apply a larger heating power. In this case, P_{\max} is ramped up to a higher power, P_{hi} . The value of P_{hi} is determined by the maximum power available from the power supply, the maximum power that the power regulator can handle, or the maximum power that is reasonable for a particular application. P_{hi} is typically much higher than P_{lo} . The purpose of the ramp is to make P_{\max} a continuous function of time: a step change in P_{\max} can disturb the tracking accuracy of the differential controller. If R_{ramp} is the resistance value at the top of the ramp, then the formula for calculating P_{\max} is

$$P_{\max} = \begin{cases} P_{lo} & \text{if } R < R_t \\ P_{lo} + \frac{(P_{hi} - P_{lo})(R - R_t)}{R_{\text{ramp}} - R_t} & \text{if } R_t \leq R < R_{\text{ramp}} \\ P_{hi} & \text{otherwise.} \end{cases} \quad (2)$$

In the experiments, the following parameters are used: $P_{lo} = 2.92 \text{ W}$, $P_{hi} = 14.4 \text{ W}$, $R_t = 85 \Omega$, and $R_{\text{ramp}} = 90 \Omega$. P_{lo} and P_{hi} correspond to current levels of 0.18 A and 0.4 A respectively.

The experimental results for $\pm 5 \text{ N}$ step commands with rapid heating are presented in Figures 11(a)–(c). The rapid-heating mechanism greatly improves the speed of response, with a rise time of only 0.1 s for a 5 N step. This corresponds to an average force rate of 50 N s^{-1} , a factor of 8 improvement compared to the experimental force rate of 6.25 N s^{-1} from Figure 8(c). Results also show no loss of tracking accuracy, as the error amplitude is still less than 0.001 N. The incorporation of the rapid-heating mechanism does not adversely affect the anti-slack mechanism, as can be seen from the 0.2 N minimum force maintained by both actuators in Figure 11(b). However, the results show peak individual forces of approximately 4.8 N on both SMA wires. This exceeds the 3 N safe force range of the SMA. The overstressing poses a problem as it can damage the actuator.

The rapid-heating mechanism also improves the tracking speed to sinusoidal commands significantly. Figures 11(d)–(e) presents a comparison between tracking responses to a 1 Hz force sinusoid without rapid heating and with the mechanism implemented. Without rapid heating, the heating current is saturated at 0.18 A, which limits the speed of response as shown in Figure 11(d). In Figure 11(e), better tracking is achieved using the larger currents allowed by the rapid-heating algorithm. Figure 11(f) shows that the control system with the rapid-heating mechanism can still accurately track a 2 Hz force command. Although no closed-loop frequency response results have been presented, the force tracking results in Figures 11(e)–(f) demonstrate that the controller’s force bandwidth is at least 2 Hz. Based on the recorded force rate of 50 N s^{-1} , higher bandwidth is achievable. However, this high-frequency tracking is only possible if the SMA wires exceed the 3 N safe force. Therefore, the controller’s bandwidth is a consequence of saturation behaviour, namely limitations in maximum heating power and force overload thresholds.

4.4 Anti-Overload Mechanism

When the differential force command is large or the rapid-heating algorithm delivers large currents to the active SMA wire, it runs the risk of overstressing. This is undesirable as it can damage the actuator. The aim of the anti-overload mechanism is to prevent overstressing of the actuator.

The anti-overload mechanism shown in Figure 12 is activated whenever the measured force of any SMA wire is greater than an upper force threshold, F_{\max} . The mechanism is a proportional feedback algorithm that determines the maximum of the forces from the individual SMA wires, compares it to the overload force threshold and appropriately reduces the power input to the actuator. The saturation block activates the anti-overload mode only if the measured maximum force is greater than F_{\max} . In the experiments, the anti-overload parameters are set to $F_{\max} = 3$, saturation limit $max = 0$, and gain $K_o = 100$. The anti-overload power is also a common-mode signal as it is delivered to both wires.

Figure 13 presents the experimental response to $\pm 5 \text{ N}$ steps with the anti-overload mechanism implemented. Two distinct slopes can be seen during the transients in Figure 13(a). The faster, first slope is due to the effects of rapid-heating. At the time when the response changes to the slower slope, it can be seen in Figure 13(b) that the individual force of the active wire has crossed the 3 N threshold. The slower slope is when the anti-overload mechanism kicks in. Note that the large force overshoots previously observed have been prevented. The results in Figure 13(b) also show rapid oscillations in the individual SMA forces when the anti-overload is activated. This indicates that the anti-overload controller is sub-optimal and requires improvement.

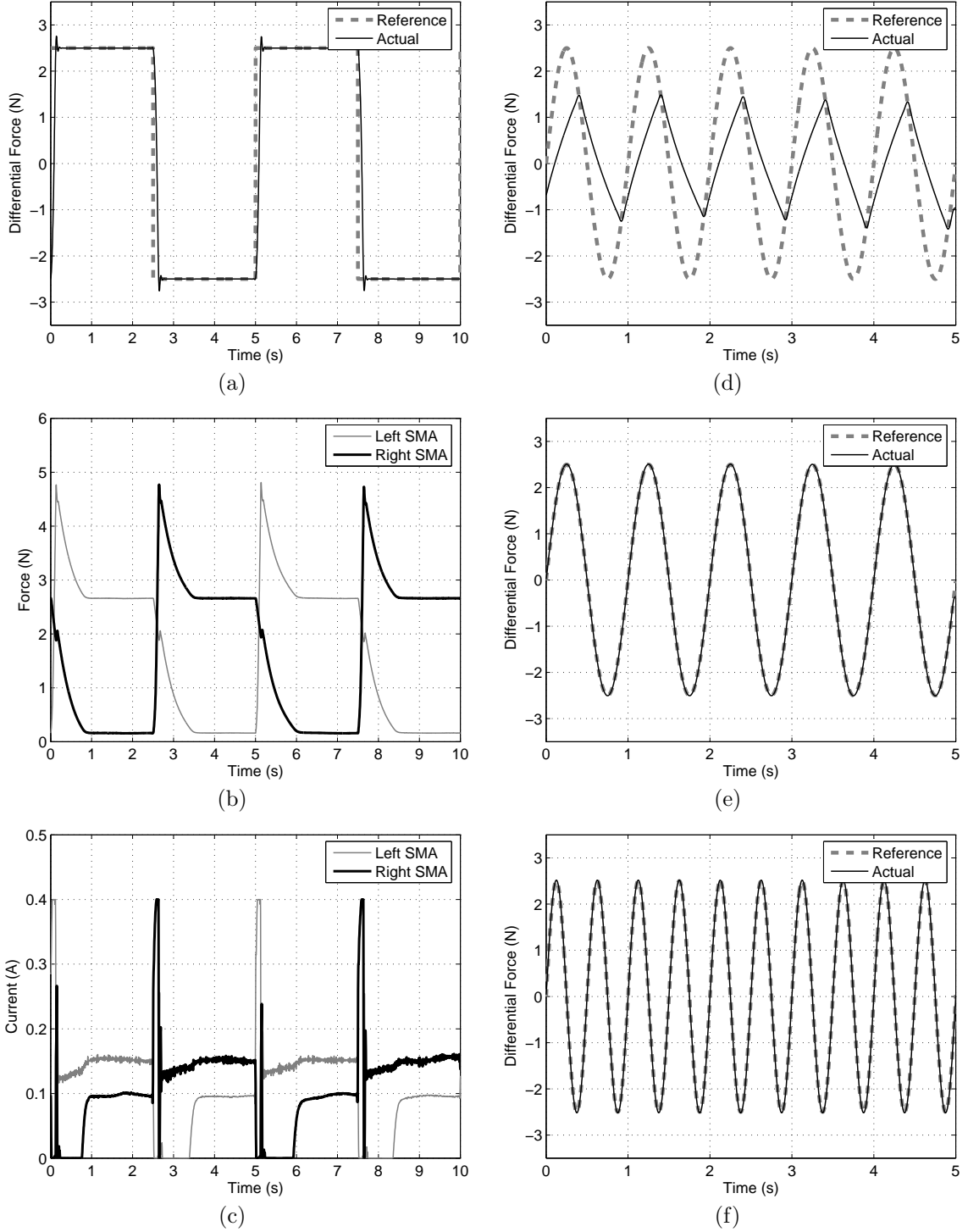


Figure 11: (a) Experimental differential force response for steps of ± 5 N with rapid-heating mechanism implemented, (b) its corresponding individual SMA forces, and (c) individual SMA heating currents. (d) Differential force tracking response at 1 Hz without rapid heating. (e) Differential force tracking response at 1 Hz with rapid heating. (f) Differential force tracking response at 2 Hz with rapid heating.

However, the experimental results continue to demonstrate excellent setpoint accuracy and the lack of limit cycles at steady-state. The results also show that the control system incorporating rapid-heating, the anti-slack and the anti-overload mechanisms can achieve fast, accurate force control without the concerns of actuator damage. Furthermore, the results clearly demonstrate the compromise between response speed and overloading. To further improve speed, perhaps a slightly larger force threshold than 3 N in the anti-overload mechanism can be used, although the exact effects on the long-term performance of the actuator, if there are

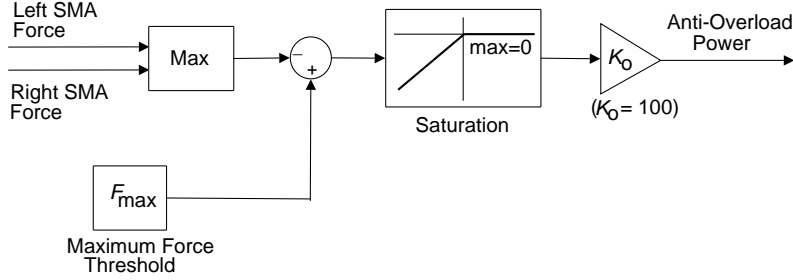


Figure 12: Anti-Overload Mechanism.

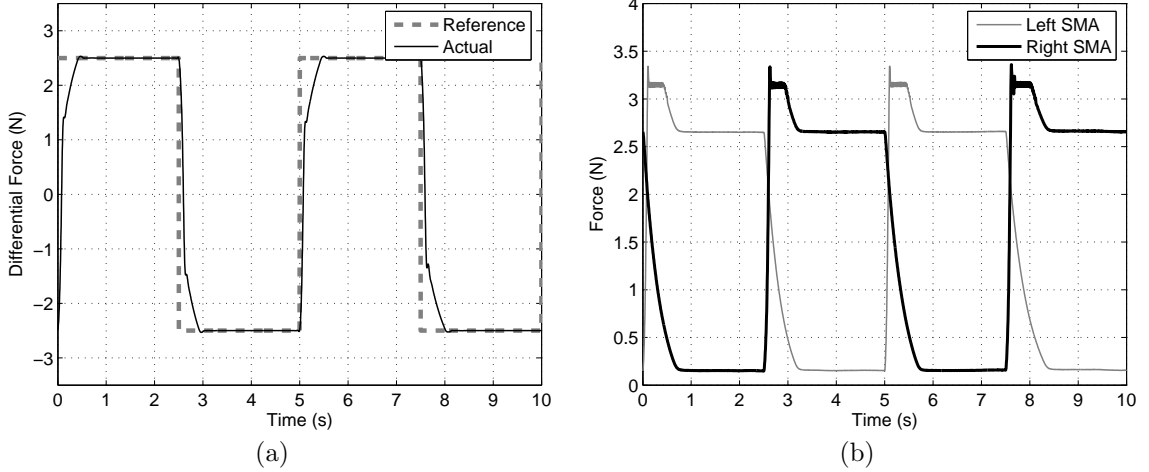


Figure 13: (a) Experimental differential force response for steps of ± 5 N with anti-overload mechanism implemented, and (b) its corresponding individual SMA forces.

any, are yet to be determined.

5 Motion Disturbance and Load Inertia Rejection

In this section, we investigate how the differential force feedback controller performs under the influence of external motion disturbances and load inertias. As a comparison, the tracking response to a trapezoidal command signal, without any external disturbances (pulley locked), is first presented in Figure 14. The ramps have slopes of $\pm 1 \text{Ns}^{-1}$ in Figure 14(a) and $\pm 2 \text{Ns}^{-1}$ in Figure 14(c). The results demonstrate excellent overall performance of the force control architecture.

To investigate the effects of external influences, two changes were made on the experimental test bed. First, the pulley is unlocked so that it is free to rotate. This allows motion disturbances (pulley rotation) to take place, and introduces large coupling effects between the antagonistic SMA wires, as the pulling force of one wire is transmitted to the other, and vice versa. The rotation of the pulley is measured using an optical encoder. Second, a load of 79g, which acts like a pendulum, is attached to the pulley. This heavy pendulum (compared to the mass of the SMA wires) is a difficult dynamic load inertia to be controlled by the system.

When the system is subjected to these influences, the results are still generally good. They are presented in Figure 15. The steady-state accuracy is maintained, but the accuracy during the ramps has been affected, with peak error amplitudes of 0.04N in Figure 15(b) and 0.08N in Figure 15(f). These spikes occur during the change of slopes, and are caused by the activation of the anti-overload mechanism. However, it can be seen that the controller can rapidly recover from these events.

Comparison between Figures 14 and 15 shows similarly good tracking responses, except for a slight degradation during the ramps and the change in slopes, which the controller can quickly correct. However, the forces on the individual wires in Figures 15(c) and 15(g) are very different from those in Figures 14(b) and 14(d). These differences can be explained as follows.

Suppose the force command is at $+2$ N, and is about to start ramping down to -2 N. Before the ramp starts, the left SMA wire is hot, and the right SMA wire is cool or cold. Also, the pendulum has come to rest at a position 15° to the right of centre (see Figures 15(d) and 15(h)), which means that the left SMA

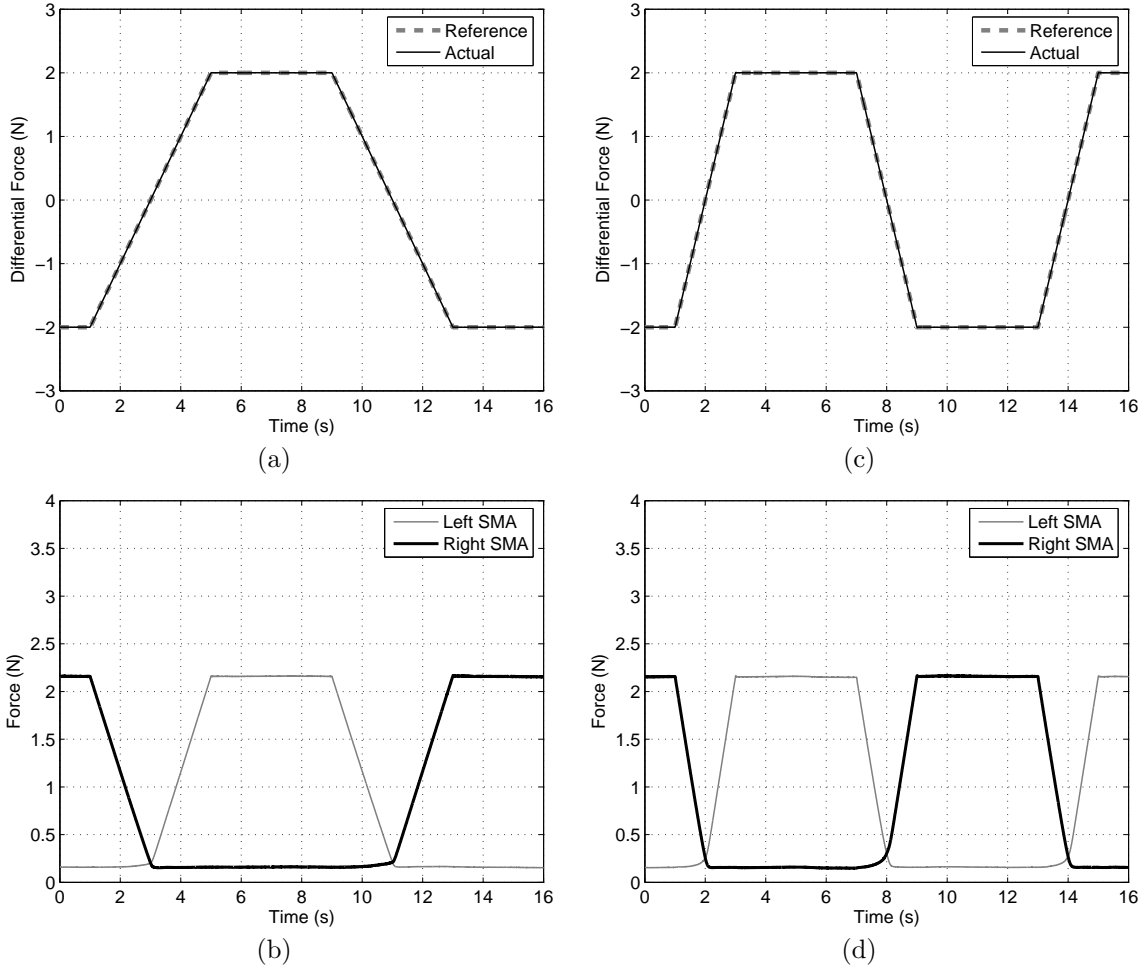


Figure 14: Experimental differential force ramp response with no external disturbances (pulley locked). (a) Differential force ramp response at ramp rates of $\pm 1\text{Ns}^{-1}$, and (b) its corresponding individual SMA forces. (c) Differential force ramp response at ramp rates of $\pm 2\text{Ns}^{-1}$, and (d) its corresponding individual SMA forces.

wire is substantially contracted, and the right SMA wire is substantially stretched. When the ramp begins, the heating power to the left SMA wire is reduced, and it begins to cool. At the same time, the pendulum begins to swing down, because the force from the actuator is reducing. This means that the left SMA is being stretched, while the stretch on the right SMA is being reduced. The latter causes the tension on the right SMA to go down, which means that the tension on the left SMA must go down even faster, so as to maintain the correct differential force. This pattern continues until the anti-slack mechanism kicks in, and stops the tension on the right SMA wire from falling below 0.2N. From here on, the tension on the left SMA wire drops gradually to the cross-over point, and then the tension on the right SMA wire, which is now the active wire, begins to rise. Towards the end of the ramp, the left SMA wire approaches its maximum extension, and begins to offer some resistance. In effect, it begins to act like a spring. It can be seen from both Figures 15(d) and 15(h) that the sudden onset of the force ramp excites the pendulum into small oscillations, which have little effect on the tracking accuracy of the force controller. These oscillations cease at the end of each ramp, probably due to a small amount of friction in the bearing.

This experiment shows that the force controller remains accurate and free from limit cycles when the actuator is connected to a heavy, moving inertial load.

6 Motion Control of Heavy Loads

A two-loop position control architecture is proposed in this section. Results show that closing the position loop, in addition to the differential force controller, produces a highly accurate SMA motion control system in the presence of heavy loads. We use the same plant in this section as was used in Section 5: a 79g pendulum attached to the pulley.

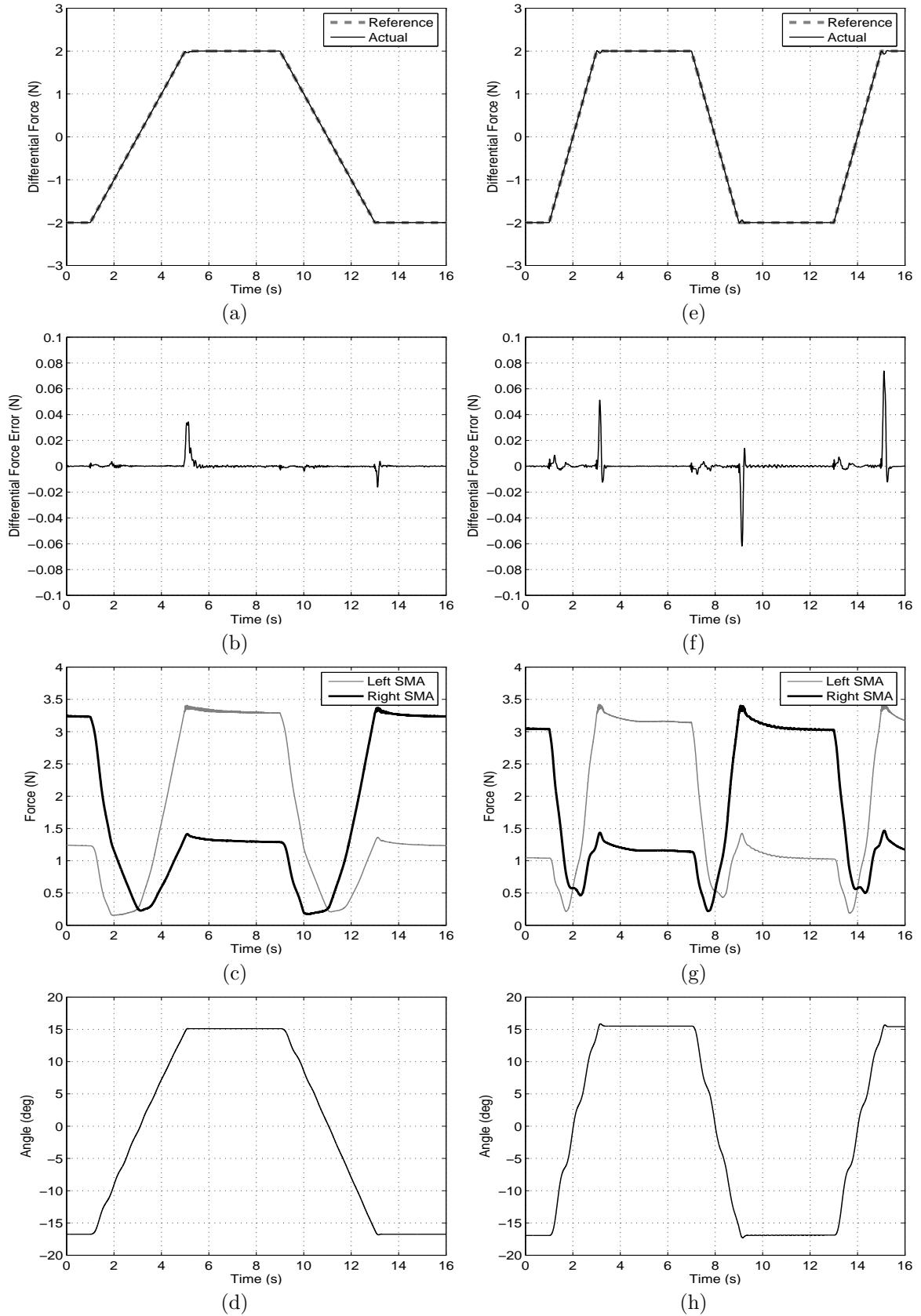


Figure 15: Experimental differential force ramp response under differential load and motion disturbances (pulley unlocked). (a) Differential force response at ramp rates of $\pm 1 \text{ N s}^{-1}$, (b) its corresponding force errors, (c) individual SMA forces, and (d) encoder position on pulley. (e) Differential force response at ramp rates of $\pm 2 \text{ N s}^{-1}$, (f) its corresponding force errors, (g) individual SMA forces, and (h) encoder position on pulley.

6.1 Two-Loop Control Architecture

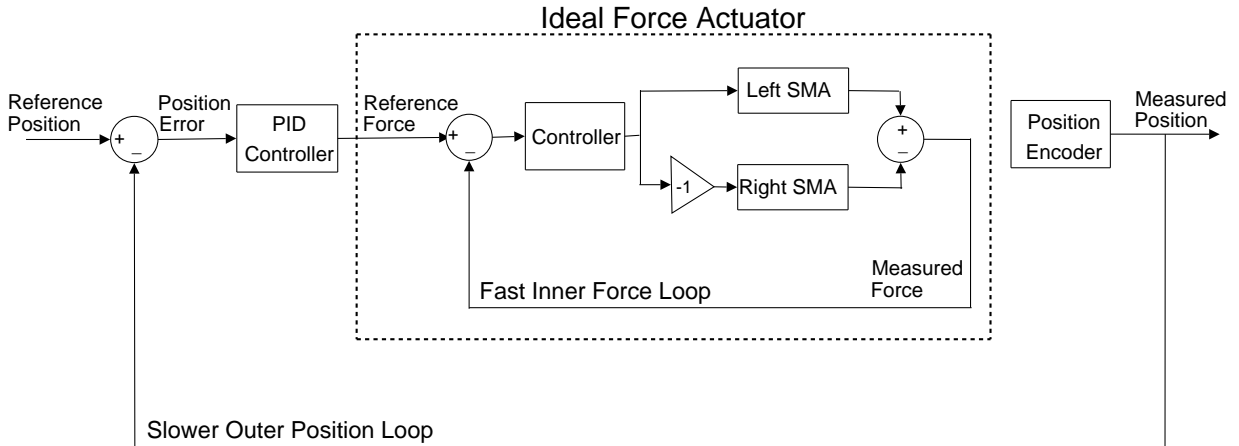


Figure 16: Motion control system with two-loop control architecture for an SMA actuator composed of an antagonistic pair of SMA wires.

The SMA motion control system adopts a two-loop control architecture as shown in Figure 16. It consists of a fast, high-bandwidth inner force loop, based on the architecture in Figure 2, and a slower, outer position loop closed around the rotation of the joint. The reasons for choosing this two-loop control architecture are summarised as follows:

1. We have high-bandwidth force sensors capable of providing highly accurate force measurements.
2. We have achieved fast, accurate differential force control of antagonistic SMA actuators with excellent motion and load disturbance rejection. This controller is suitable for use as the inner force loop.
3. With the inner differential force controller, the antagonistic SMA actuators can be assumed to behave like an ideal force actuator. So whatever force commands are required within the possible range of the actuators, the inner force loop can be expected to quickly achieve the desired setpoint or response with high accuracy, and no limit cycles or steady-state errors.
4. We believe that it can eliminate limit cycles and compensate for external load disturbances.

Note that the rapid-heating, the anti-slack and the anti-overload mechanisms are always implemented in the inner differential force loop although not shown in the simplified diagram of Figure 16. The outer position loop also implements a PID controller which has been tuned with $K_P = 0.5$, $T_I = 0.1$ and $T_D = 0.06$.

6.2 Results and Discussions

The two-loop motion control system is tested under an external load of 79 g. Figure 17 presents the experimental results to both step and sine commands. A maximum P_{hi} of 14.4 W in the rapid heating mechanism, corresponding to a current of 0.4 A, is applied across all experiments.

With the two-loop motion control system, the limit cycle problem has been eliminated. Firstly, the step response in Figure 17(a) demonstrates moderate speed response to $\pm 20^\circ$ steps, with a rise time of 0.2 s and a settling time of approximately 1 s. However, there are no observed limit cycles, setpoint tracking is stable, and the position errors at steady-state are smaller than the resolution of the position encoder. Figure 17(b) presents the individual SMA forces measured during the step response experiment. The transient force responses clearly show fast dynamics from the actuators and the external load. Note that the anti-overload force threshold, F_{max} , is set very high at 6 N.

The sine response of Figure 17(c) shows stable tracking with no sign of limit cycles under heavy inertial loads. However, it can be seen that the peak magnitudes of the 1 Hz sine command have not been tracked. This is due to the low gains used in the position PID controller. It can also be observed that the average SMA forces are quite high, at more than 2 N generally in Figure 17(d). This is due to the stretching of the passive (less heated) wire. Also, the observed drifts in SMA forces are due to air movement around the actuators.

The two-loop motion control system demonstrates accurate and stable tracking in the presence of heavy external loads. There are no limit cycles or steady-state errors, unlike the results observed by Grant (1999), Teh and Featherstone (2004) and Van der Wijst (1998) using only position feedback control. The anti-overload

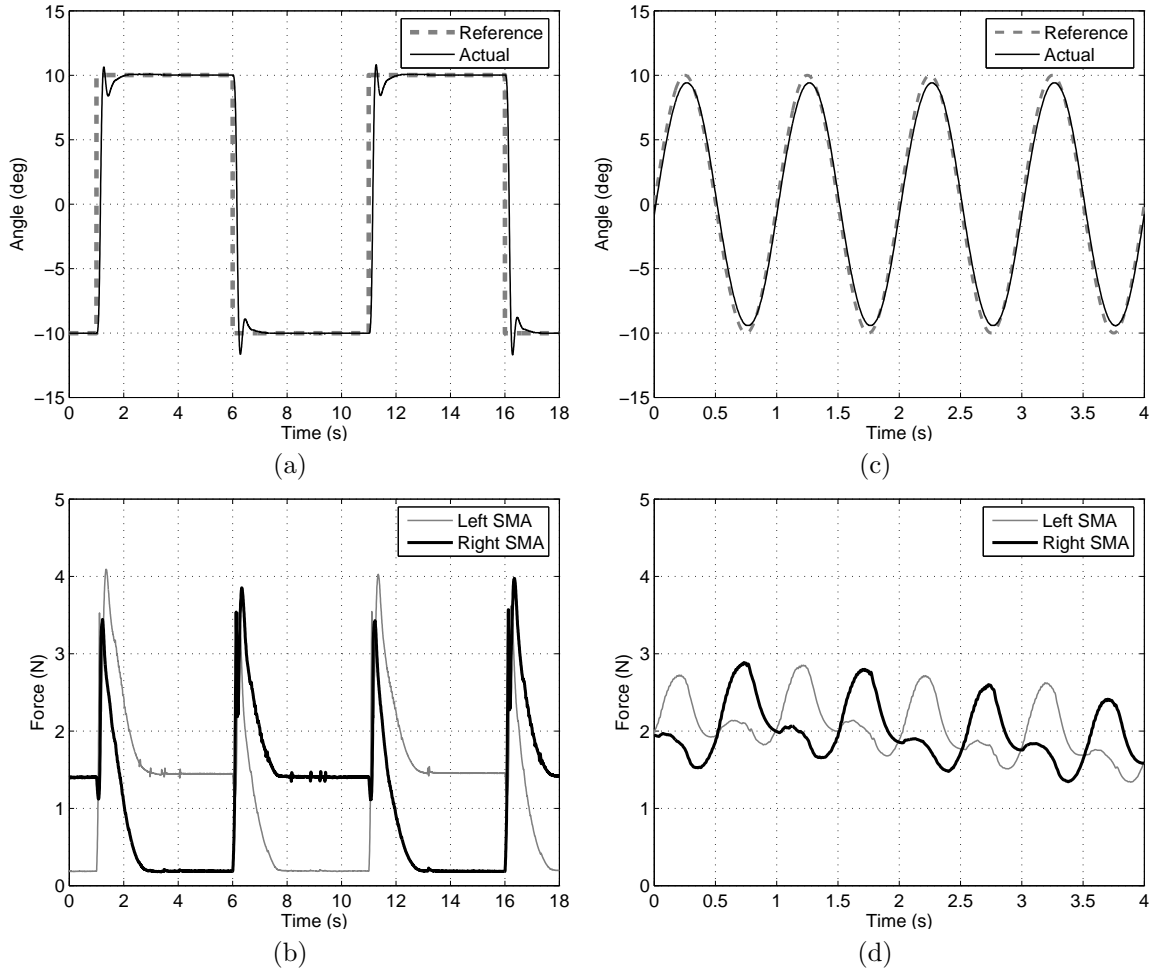


Figure 17: Experimental motion control results with two-loop control (with external load of 79g). (a) Position step response, and (b) its corresponding individual SMA forces. (c) Position tracking response at 1Hz, and (d) its corresponding individual SMA forces.

and rapid-heating mechanisms can protect the SMA actuator from overstressing and overheating of the wires, which other controllers in the literature do not.

7 Conclusions

A force control system has been presented that produces fast, accurate responses in an actuator consisting of an antagonistic pair of SMA wires. The differential force control system consists of a PID differential controller and three additional control elements — the anti-slack, the rapid-heating and the anti-overload mechanisms. The force response demonstrates the following characteristics:

1. Fast tracking with a high average force rate of 50Ns^{-1}
2. Setpoint accuracy as high as 0.001N , which is 0.017% of the 6N output force range
3. No limit cycles observed
4. Actuator damage prevented with no overheating or overstressing of SMA wires
5. Good external disturbance rejection

This paper also describes a position controller, which is formed by closing an outer position feedback loop around the force controller. This control system, in the presence of heavy dynamic loads, demonstrates highly accurate positioning, with no limit cycles and no measurable steady-state errors. However, based on the results presented, the position tracking speed of our two-loop controller is not as fast as the force tracking speed.

The results achieved in this research can be used as guidelines for enabling practical SMA actuator and robotic applications. Future research directions include implementing better control designs to further improve

the speed of response of the SMA actuator. We plan to investigate using larger thresholds in rapid heating and the anti-overload mechanism. A more effective anti-overload scheme will also be investigated.

References

- Ashrafioun, H., Eshraghi, M., and Elahinia, M. H. (2006). Position Control of a 3-Link Shape Memory Alloy Actuated Robot. *J. Intelligent Material Systems & Structures*, vol. 17, pp. 381–392.
- Bergamasco, M., Dario, P., and Salsedo, F. (1990). Shape Memory Alloy Microactuators. *Sensors & Actuators A: Physical*, vol. 21, no. 1-3, pp. 253–257.
- Choi, S. B., Han, Y. M., Kim, J. H., and Cheong, C. C. (2001). Force Tracking Control of a Flexible Gripper Featuring Shape Memory Alloy Actuators. *Mechatronics*, vol. 11, pp. 677–690.
- Dickinson, C. A., and Wen, J. T. (1998). Feedback Control Using Shape Memory Alloy Actuators. *J. Intelligent Material Systems & Structures*, vol. 9, no. 4, pp. 242–250.
- Dynalloy, Inc. (Last accessed 10 December 2007). Flexinol® Technical Data. <http://www.dynalloy.com/TechnicalData.html>
- Elahinia, M. H., and Ashrafioun, H. (2002). Nonlinear Control of a Shape Memory Alloy Actuated Manipulator. *J. Vibration & Acoustics, Transactions of the ASME*, vol. 124, pp. 566–575.
- Featherstone, R., and Teh, Y. H. (2004). Improving the Speed of Shape Memory Alloy Actuators by Faster Electrical Heating. Proc. 9th Int. Symp. Experimental Robotics, Singapore, June 18–21, paper ID 128.
- Featherstone, R., and Teh, Y. H. (2005). A Shape Memory Alloy Actuator. International patent application no. PCT/AU2005/000154.
- Featherstone, R., and Teh, Y. H. (2006). A Shape Memory Alloy Actuator. Australian patent application no. 2005210682.
- Fu, Y., Du, H., Huang, W., Zhang, S., and Hu, M. (2004). TiNi-based Thin Films in MEMS Applications: A Review. *Sensors & Actuators A: Physical*, vol. 112, no. 2-3, pp. 395–408.
- Gorbet, R. B., and Russell, R. A. (1995). A Novel Differential Shape Memory Alloy Actuator for Position Control. *Robotica*, vol. 13, pp. 423–430.
- Grant, D., and Hayward, V. (1997). Controller for a High Strain Shape Memory Alloy Actuator: Quenching of Limit Cycles. Proc. IEEE Int. Conf. Robotics & Automation, vol. 1, pp. 254–259.
- Grant, D., and Hayward, V. (1997). Variable Structure Control of Shape Memory Alloy Actuators. *IEEE Systems and Control Magazine*, vol. 9, no. 3, pp. 80–88.
- Grant, D., and Hayward, V. (2000). Constrained Force Control of Shape Memory Alloy Actuators. Proc. IEEE Int. Conf. Robotics & Automation, vol. 2, pp. 1314–1320.
- Grant, D. (1999). Accurate and Rapid Control of Shape Memory Alloy Actuators. Ph.D. Thesis, McGill University.
- Hunter, I. W., Lafontaine, S., Hollerbach, J. M., and Hunter, P. J. (1991). Fast Reversible NiTi Fibers for Use in Microrobotics. Micro Electro Mechanical Systems, 1991, MEMS '91, Proc. 'An Investigation of Micro Structures, Sensors, Actuators, Machines and Robots', pp. 166–170.
- Ikuta, K., Tsukamoto, M., and Hirose, S. (1988). Shape Memory Alloy Servo Actuator System with Electric Resistance Feedback and Application for Active Endoscope. Proc. IEEE Int. Conf. Robotics & Automation, vol. 1, pp. 427–430.
- Kohl, M. (2004). Shape Memory Microactuators. Springer-Verlag, Berlin Heidelberg.
- Kuribayashi, K. (1991). Improvement of the Response of an SMA Actuator Using a Temperature Sensor. *Int. J. Robotics Research*, vol. 10, no. 1, pp. 13–20.
- Liang, C., and Rogers, C. A. (1993). Design of Shape Memory Alloy Springs with Applications in Vibration Control. *J. Vibration & Acoustics*, vol. 115, pp. 129–135.

- Madill, D. R., and Wang, D. (1998). Modeling and L2-Stability of a Shape Memory Alloy Position Control System. *IEEE Trans. Control Systems Technology*, vol. 6, no. 4, pp. 473–481.
- Moallem, M., and Lu, J. (2005). Application of Shape Memory Alloy Actuators for Flexure Control: Theory and Experiments. *IEEE/ASME Trans. Mechatronics*, vol. 10, no. 5, pp. 495–501.
- Mosley, M. J., and Mavroidis, C. (2001). Experimental Nonlinear Dynamics of a Shape Memory Alloy Wire Bundle Actuator. *Trans. ASME, J. Dynamic Systems, Measurement & Control*, vol. 123, no. 1, pp. 103–112.
- Russell, R. A., and Gorbet, R. B. (1995). Improving the Response of SMA Actuators. Proc. IEEE Int. Conf. Robotics & Automation, vol. 3, pp. 2299–2304.
- Teh, Y. H., and Featherstone, R. (2004). Experiments on the Performance of a 2-DOF Pantograph Robot Actuated by Shape Memory Alloy Wires. Proc. Australasian Conf. Robotics & Automation, Canberra, Australia, Dec. 6–8.
- Teh, Y. H., and Featherstone, R. (2005). Experiments on the Audio Frequency Response of Shape Memory Alloy Actuators. Proc. Australasian Conf. Robotics & Automation, Sydney, Australia, Dec. 5–7.
- Teh, Y. H., and Featherstone, R. (2007a). Accurate Force Control and Motion Disturbance Rejection for Shape Memory Alloy Actuators. Proc. IEEE Int. Conf. Robotics & Automation, Rome, Italy, Apr. 10–14.
- Teh, Y. H., and Featherstone, R. (2007b). Frequency Response Analysis of Shape Memory Alloy Actuators. Proc. Int. Conf. Smart Materials & Nanotechnology in Engr. Harbin, China, Jul. 1–4.
- Teh, Y. H. (2007). Fast, Accurate Force and Motion Control of Shape Memory Alloy Actuators. Ph.D. Thesis, Dept. Information Engineering, The Australian National University, Canberra, Australia, (Submitted 31 October 2007).
- Troisfontaine, N., Bidaud, P., and Dario, P. (1997). Control Experiments on Two SMA Based Micro-Actuators. Proc. Fifth Int. Symp. Experimental Robotics, Springer-Verlag, pp. 490–499.
- Van der Wijst, M. (1998). Shape Control of Structure and Materials with Shape Memory Alloys. Ph.D. Thesis, Technische Universiteit Eindhoven.
- Van Humbeeck, J. (1999). Non-Medical Applications of Shape Memory Alloys. *Materials Science & Engineering A*, vol. 273–275, pp. 134–148.
- Waram, T. (1993). Actuator Design Using Shape Memory Alloys. T. C. Waram, 2nd (Metric) Edition, Ontario, Canada.
- Zhong, Z. W., and Yeong, C. K. (2006). Development of a Gripper using SMA Wire. *Sensors & Actuators A: Physical*, vol. 126, pp. 375–381.